JOURNAL OF SPACECRAFT AND ROCKETS
Vol. 45, No. 4, July–August 2008

Viscous Effects on Performance of Two-Dimensional Supersonic Linear Micronozzles

William F. Louisos* and Darren L. Hitt†
University of Vermont, Burlington, Vermont 05405

DOI: 10.2514/1.33434

A comprehensive numerical investigation of a steady viscous flow through a two-dimensional supersonic linear micronozzle has been performed. The baseline model for the study is derived from the NASA Goddard Space Flight Center microelectromechanical systems-based hydrogen peroxide prototype microthruster. On the microscale, substantial viscous subsonic layers may form on the nozzle expander walls, which reduce thrust and efficiency. One approach to compensate for the presence of these layers has been to design micronozzles with expansion angles larger than traditional macroscale nozzles. Numerical simulations have been conducted for a range of Reynolds numbers (Re = 15–800) and for expander half-angles of 10–50 deg. Two different monopropellant fuels have been considered: decomposed 85% pure hydrogen peroxide and decomposed hydrazine. It is found that an inherent tradeoff exists between the viscous losses and the losses resulting from the nonaxial exit flow at larger expansion angles. Our simulations indicate that the maximum nozzle efficiency occurs for both monopropellants at a nozzle expansion half-angle of approximately 30 deg, which is significantly larger than that of traditional conical nozzle designs.

Nomenclature

A	=	area, m^2
$\mathbf{F}$	=	thrust, N
g	=	gravity, m/s^2
I_{sp}	=	specific impulse, s
L	=	characteristic length scale, m
$\dot{m}$	=	mass flow rate, kg/s
p	=	pressure, Pa
R	=	gas constant, $\frac{J}{kgK}$
Re	=	Reynolds number
T	=	static temperature, K
$\mathbf{u}$	=	velocity, m/s
γ	=	ratio of specific heats
η	=	nozzle efficiency, %
θ	=	expander half-angle, deg
μ	=	viscosity, $\frac{kg}{m^2 \cdot s}$
ρ	=	density, kg/m^3

Subscripts

exit	=	nozzle exit conditions
0	=	stagnation condition
∞	=	ambient condition

Superscripts

*	=	throat condition
opt	=	optimal condition

I. Introduction

MICROELECTROMECHANICAL systems (MEMS) techniques offer great potential in satisfying future mission requirements for the next generation of small scale spacecraft being designed by NASA and the Department of Defense agencies. These nano-sized spacecraft, more commonly referred to as "nanosats," feature masses in the range of 1–20 kg. Owing to the substantially reduced size, the nano-sized satellites have unique propulsion requirements, including extremely low thrust levels and/or extremely low minimum impulse requirements for orbital maneuvers and attitude control [1,2]. Recent surveys of micropropulsion systems for formation flying applications and microthruster options can be found in the reviews by Mueller [3] and Reichbach et al. [4].

A key component in microthruster design based upon either solid or chemical propellants is the converging–diverging supersonic nozzle. In designing a MEMS-based supersonic nozzle, however, there are certain considerations unique to the microscale that must be addressed. First, owing to the inherent nature of microfabrication techniques (e.g., reactive ion etching, wet etching), the resulting nozzles are ducts with rectangular cross sections and so are *not axisymmetric* like their macroscale counterparts. Macroscale thrusters often feature outlet nozzles with contoured walls (e.g., "bell" or "trumpet" shapes) for the purposes of straightening the outlet flow and producing a uniaxial thrust normal to the exit plane. Microfabrication of such symmetric wall contours is generally difficult especially in terms of reproducibility; as a result, the current trend is to design a linear micronozzle having straight walls with a specified expansion half-angle θ. The micronozzle geometry is a 2-D pattern that is etched into a silicon wafer or other substrate material. Depending on the microfabrication technique implemented, micronozzle depths typically range from 10–300 μm. The result is a 3-D micronozzle with a rectangular cross section. Figure 1 shows the geometry of a prototype MEMS-based monopropellant microthruster developed at NASA Goddard Space Flight Center (GSFC) [5] in collaboration with the University of Vermont. The converging–diverging nozzle section of the thruster, which provides the basis and motivation for the present study, has been outlined for clarification.

The intent of this study is to characterize micronozzle performance for a range of flow conditions and expander geometries for a simplified 2-D micronozzle model. Specifically, we seek to identify and understand the conditions that maximize the thrust production and nozzle efficiency. There exist several key factors to be analyzed in the study of micronozzle flow that ultimately affect performance characteristics. The flow in a MEMS supersonic nozzle can be substantially affected by viscous effects. For various microscale nozzles reported in the literature, the Reynolds numbers are relatively low; typical values are well below 1000 and some are less

Presented as Paper 5032 at the AIAA Fluid Dynamics Conference, Toronto, Canada, 6–9 June 2005; received 13 July 2007; revision received 17 January 2008; accepted for publication 24 February 2008.

*Ph.D. Candidate in Mechanical Engineering, School of Engineering, 301 Votey Hall, 33 Colchester Avenue.

†Associate Professor of Mechanical Engineering, School of Engineering, 301 Votey Hall, 33 Colchester Avenue.

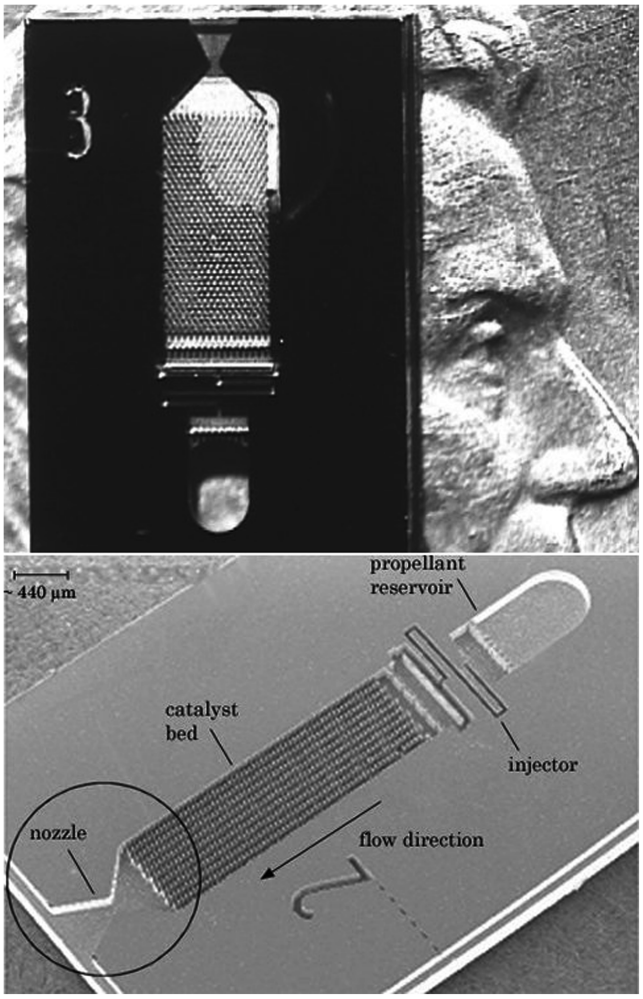

Fig. 1 NASA GSFC microthruster: a) photograph of the NASA GSFC MEMS-based microthruster etched into a silicon wafer and placed on top of a U.S. penny for reference [5], and b) scanning electron microscopy image of the NASA GSFC microthruster with the converging–diverging supersonic micronozzle outlined for clarity.

than 100. As such, the magnitude of viscous losses can be significant. In the diverging nozzle section, a viscous subsonic layer may extend a sufficient distance away from the wall so as to retard the bulk flow and reduce efficiency. To compensate for this, some designs have proposed increased expander angles; however, this introduces potential performance reductions due to nonaxial exit flow.

The viscous effects in supersonic micronozzle flow were first investigated by Bayt and Breuer [6,7], who demonstrated that the viscous boundary layer can occupy a significant portion of the nozzle area, reducing flow and resulting in thrust loss. Alexeenko et al. [8–13] and Ketsdever et al. [14] have performed extensive direct simulation Monte Carlo (DSMC) simulations of micronozzle flow for cold gas thrusters with 2-D axisymmetric and, to a lesser degree, 3-D geometries. The primary limitation of this body of work is that it has not explored a complete range of potential flow conditions (e.g., Reynolds numbers) and varying nozzle geometries. In this regard, our present study nicely complements the existing body of work.

The effects of the geometry and reduced ambient back pressure on micronozzle flows have been explored by Choudhuri et al. [15] for conical 15- and 20-deg bell- and trumpet-shaped diverging nozzle sections. Experimental studies were performed and color Schlieren imaging was used to visualize the flow regime inside the nozzle. It was shown that the flow regime in a micronozzle is highly viscous dominated, and that viscous effects play a key role in thruster performance.

In this paper, we report the key findings from extensive numerical simulations of 2-D micronozzle flows over a range of Reynolds numbers (15–800) with varying expander half-angles from $\theta =$ 10–50 deg while considering both decomposed hydrogen peroxide (H_2O_2) and decomposed hydrazine (N_2H_4) as the working monopropellants. The behavior of chemical monopropellants has not yet been considered in micronozzle flows. The combination of extensive parametric studies (Re, θ) and the incorporation of realistic monopropellants thus represents a unique and important contribution to the existing micronozzle literature. We demonstrate that an inherent tradeoff exists between the viscous effects and nozzle geometry resulting in an optimum thrust production at an expander half-angle of $\sim$30 deg for both of the monopropellants considered.

The use of a 2-D model in this work is intended as an enabling approximation. Although 3-D geometries with rectangular cross sections represent the most accurate model of current and future MEMS nozzles, the associated simulations are extremely expensive in terms of computational resources. This, in turn, renders comprehensive parametric case studies difficult and/or impractical. A 2-D model is capable of capturing much of the important phenomena associated with varying expander angles and Reynolds numbers, save for the impact of the upper and lower boundaries. The effect of a finite depth will be to reduce the nozzle performance because additional viscous layers will form on the upper/lower solid surfaces. These surfaces are flat, and the only additional design parameter introduced in the 3-D case is the depth. It is evident that a "deep" nozzle design is desirable to minimize the upper/lower surface effects, and many proposed MEMS nozzle designs involve the use of deep reactive ion etching to achieve depths of 100–300 μm or more. As the depth dimension is increased, the validity of the 2-D approximation improves. In summary, it is our assertion that the present 2-D study strikes a balance between providing comprehensive information describing micronozzle performance trends for different geometries, monopropellants, and Re at the cost of acceptable limitations in the actual device modeling.

II. Computational Model

In this study, we focus our attention on the performance of monopropellant-based microthrusters. In particular, we consider both decomposed hydrogen peroxide (H_2O_2) and decomposed hydrazine (N_2H_4) as potential monopropellants. A monopropellant scheme is attractive for micropropulsion owing to the relatively high energy density and simplicity of implementation. Hydrogen peroxide is considered a "green" monopropellant and has been chosen for the development process based on its nontoxicity and relative ease of handling. The decomposition of the H_2O_2 monopropellant occurs in a catalytic chamber upstream of the nozzle according to the one-step reaction

$$2H_2O_2 \rightarrow 2H_2O + O_2 + \text{heat} \tag{1}$$

Hydrazine offers somewhat higher specific impulse values and decades of proven use in traditional macroscale thrusters. For N_2H_4, the reaction occurs in a two-step process according to

$$3N_2H_4 \rightarrow 4NH_3 + N_2 + \text{heat} \tag{2}$$

$$4NH_3 \rightarrow 2N_2 + 6H_2 \tag{3}$$

It is worthwhile to mention here that for silicon-based MEMS devices the use of hydrazine may present material compatibility issues. Ongoing research into new erosion-resistant materials (e.g., silicon dioxide) and new nonsilicon-based MEMS materials may mitigate these problems, however [16]. In light of this, and as the present work makes no specific assumptions regarding a silicon-based substrate, the consideration of this traditional and proven monopropellant remains warranted.

The micronozzle inlet gas temperature is assumed to be that of the fully decomposed adiabatic flame temperature of 85% pure decomposed H_2O_2 (886 K). The same inlet temperature is used for the N_2H_4 simulations because the flame temperature of fully decomposed N_2H_4 is quite similar. This adiabatic flame temperature,

or stagnation temperature T_0, along with a specified stagnation pressure p_0, establishes the inlet pressure boundary condition for the micronozzle simulations. The working fluid is treated as a homogeneous, frozen mixture whose thermophysical properties are determined via a mass weighted average of the individual component properties of the decomposed monopropellant [17]. The corresponding Reynolds number for the flow is

$$Re \equiv \frac{\dot{m}L}{\mu A} \tag{4}$$

where $\dot{m}$ is the mass flow ratio per unit depth, L is the characteristic length scale (e.g., the 90 μm nozzle throat diameter), μ is the dynamic viscosity of the decomposed monopropellant, and A is the cross-sectional area. The value of $\dot{m}$ can be well estimated from quasi-1-D theory according to Anderson [18]:

$$\dot{m} = \frac{p_0 A^*}{\sqrt{T_0}} \sqrt{\frac{\gamma}{R}\left(\frac{2}{\gamma+1}\right)^{(\gamma+1)/(\gamma-1)}} \tag{5}$$

where A^* is the nozzle throat area, γ is the ratio of specific heats, and R is the universal gas constant.

A. Numerical Implementation

1. Grid Construction

The computational domains are based upon the typical nozzle geometries of the microthruster prototype developed at NASA GSFC and described in Hitt et al. [5]. The expander half-angle θ is varied between 10 and 50 deg in 2.5-deg increments; all other geometric parameters are held constant as shown in Fig. 2. The two-dimensional meshes have been developed using Fluent, Inc.'s GAMBIT 2.1 grid generation software. The throat and exit dimensions of the NASA GSFC prototype (90 μm and 560 μm, respectively) yield an area expansion ratio of 56:9 and are a fixed parameter in this study. To maintain the constant area expansion ratio as the expander half-angle varies, the axial length of the expander section is adjusted in an appropriate fashion. The mesh varies in size between 45,000 and 75,000 total elements depending on the expander angle. All of the mesh elements are quadrilateral with a maximum skewness of 0.5 occurring in less than 4.7% of the elements. The planar symmetry is also used to reduce the computational expenditure. In developing the final meshes, a systematic grid refinement study has been undertaken to ensure that all results are insensitive to further grid refinement. The refinement study examined grid insensitivity at both the low and high ends of the flow regime (Re) considered in this study. Evidence of the grid insensitivity is provided in Table 1.

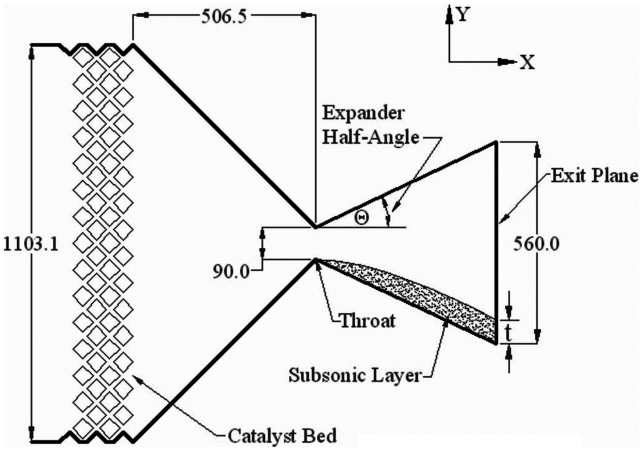

Fig. 2 2-D geometry of the NASA/GSFC monopropellant converging–diverging microthruster nozzle. Note the expander half-angle θ. All dimensions are shown in microns. The viscous subsonic boundary layer is shown schematically where t is the subsonic layer at the micronozzle exit.

Table 1 Computed values of the percentage change in the mass flux and thrust at the final stage of the grid refinement for $Re = 60, 100$. The data are for hydrogen peroxide monopropellant and a 30-deg expander half-angle

	$Re = 60$	$Re = 800$
% variation in thrust	0.0136	3.36×10^{-4}
% variation in $\dot{m}$	0.0044	8.45×10^{-4}

2. Continuum Modeling and Boundary Conditions

A continuum flow model is assumed for the operating conditions of this study. The subsonic portions of the outlet boundaries are prescribed a constant back-pressure value of 1.0 kPa. This value serves to maintain the Knudsen number within the continuum regime with the possible exception of some slip conditions at the walls for the lowest Reynolds numbers considered. For the supersonic portions of the domain outlet, the pressure and all other flow quantities are extrapolated from the interior flow via the method of characteristics (Riemann invariants). The 2-D flowfield in the micronozzle is governed by the conservation equations of mass, momentum, and energy for the fluid mixture according to

$$\frac{\partial}{\partial t}\rho + \nabla \cdot (\rho \mathbf{V}) = 0 \tag{6}$$

$$\frac{\partial}{\partial t}(\rho \mathbf{V}) + \nabla \cdot (\rho \mathbf{V}\mathbf{V}) = -\nabla p + \nabla \cdot (\boldsymbol{\tau}) \tag{7}$$

$$\frac{\partial}{\partial t}(\rho E) + \nabla \cdot (\mathbf{V}(\rho E + p)) = \nabla \cdot (k \nabla T + (\boldsymbol{\tau} \cdot \mathbf{V})) \tag{8}$$

$$E = h - \frac{p}{\rho} + \frac{\mathbf{V}^2}{2} \tag{9}$$

$$\boldsymbol{\tau} = \mu((\nabla \mathbf{V} + \nabla \mathbf{V}^T) - \tfrac{2}{3}\nabla \cdot \mathbf{V}\mathbf{I}) \tag{10}$$

In these equations ρ is the fluid density, $\mathbf{V}$ is the velocity vector, p is the absolute local pressure, E is the total energy, μ is the fluid viscosity, k is the thermal conductivity, T is the static temperature, h is the enthalpy, and $\boldsymbol{\tau}$ is the viscous stress tensor. The system of equations is closed by the ideal gas law equation of state

$$p = \rho R T \tag{11}$$

The micronozzle wall is modeled as being adiabatic. This can be justified as follows. The operation of the micronozzle as a component in a micropropulsion system is inherently of limited, and often quite short, duration (perhaps $\ll 1$ s). This is not inconsistent with our steady-state assumption as the nozzle flow response time to a valve actuation can be extremely short on the microscale: less than 1 ms. In contrast, the time scale associated with heat transfer through the boundary is substantially longer. Thus, it is quite reasonable to regard the process as adiabatic. This notion is supported by the results in Alexeenko et al. [13].

Initial simulations were performed under the assumption of a no-slip boundary condition. A posteriori calculations of the Knudsen number obtained from the initial simulation data showed values of $Kn < 0.01$ within the nozzle region for the moderate to high Reynolds numbers examined and, thus, was consistent with the no-slip assumption. However, calculations for the lowest Reynolds numbers indicated localized values of Kn that were typically associated with the wall slip regime. As a reference for the reader, the average Knudsen number has been computed along the length of the expander wall ($\overline{Kn}$) and appears in Table 2. To further examine the significance of possible wall slip, a new set of calculations were

Table 2 Average Knudsen number values along the nozzle expander wall and the percent difference between the no-slip and slip simulations for selected Reynolds numbers. The data here are for hydrogen peroxide monopropellant and a 30-deg expander half-angle

Re	$\bar{Kn}$	% difference—thrust	% difference—mass flux
15	0.0548	1.50	2.0
60	0.0290	0.94	1.9
800	0.0031	0.451	0.0016

performed by imposing first-order slip conditions. A tangential momentum accommodation coefficient of 0.85 was chosen based on experimental data for highly polished silicon [19]. Comparisons of the predicted thrust and mass fluxes for the slip and no-slip cases are summarized in Table 2. It is seen that the differences in the thrust prediction are at most 1.5% at the lowest of the flow rates and below 1% for all other scenarios. These modest differences correspond to the ideal case of highly polished silicon surfaces. In an actual device, the presence of surface roughnesses, be they the result of fabrication limitations or surface contamination, would reduce the impact of slip, and one would expect behavior approaching no-slip boundaries. On these grounds, we have opted to impose no-slip conditions for all of the case simulations.

3. *Computational Schemes*

The initial guess for the solution is applied to the domain based on quasi-1-D inviscid theory. A coupled-implicit solver is used with a second-order upwind discretization scheme for the convective terms. The steady-state solutions are obtained using a pseudo-time-stepping procedure, and convergence of the solution is assessed via residuals and point monitors for key flow quantities (e.g., $\dot{m}$) at selected locations within the domain. Comparisons to relevant data in the micronozzle literature will be considered later in this paper.

B. Thrust and Efficiency

In this study, we are concerned with evaluating the thrust production and nozzle efficiency for the cases examined. The thrust is formally calculated from the simulation data according to

$$\mathbf{F} = \int_{A_{\text{exit}}} \rho u(\mathbf{u}\cdot\mathbf{n})\,\mathrm{d}A + \int_{A_{\text{exit}}} (p_{\text{exit}} - p_\infty)\,\mathrm{d}A \tag{12}$$

where p_{exit} is the pressure at the exit plane of the nozzle and p_∞ is the ambient back pressure. In our simulations, however, the pressure thrust term is negligible in comparison to the momentum thrust.

Another quantity of interest is the nozzle efficiency η, which can be defined as the ratio of the realized specific impulse (I_{sp}) to the idealized specific impulse ($I_{\text{sp}}^{\text{opt}}$) for a given pressure ratio (p_{exit}/p_0) across the nozzle [20]:

$$\eta = \frac{I_{\text{sp}}}{I_{\text{sp}}^{\text{opt}}} = \frac{\mathbf{F}/(\dot{m}g)}{\sqrt{\frac{2\gamma RT_0}{g^2(\gamma-1)}\left[1-\left(\frac{p_{\text{exit}}}{p_0}\right)^{\gamma/(\gamma-1)}\right]}} \tag{13}$$

where g is the acceleration due to gravity and $\mathbf{F}$ is the thrust production as given by Eq. (12).

III. Numerical Results

In this section, we first present the performance results and a subsonic layer analyses for the underexpanded micronozzle flows with varying expander half-angles at a fixed throat Reynolds number of $Re \sim 800$ for both monopropellants of interest; results for certain cases of perfectly expanded nozzle flow are also described for comparison. We then present results from a Reynolds number parametric study ($Re = 15$–800) for the same set of expander geometries with decomposed H_2O_2 as the working fluid mixture. Finally, we discuss the nature of the temperature-dependant thermophysical properties and their impact on the boundary-layer size and micronozzle performance.

A. Nozzle Performance for Varying Expander Angles

Here we present results from a parametric study of micronozzle performance for varying expander half-angles. An inlet pressure p_0 of 250 kPa is imposed on the inlet boundary and yields a corresponding throat Reynolds number of $Re \sim 800$. This value has been chosen based on the original NASA GSFC design, whose target thrust levels were in the range of 1–20 μN. An illustrative example of the Mach contours and streamlines are depicted in Fig. 3 for the 15- and 45-deg expanders with a flow of decomposed H_2O_2. For these inlet conditions, the exit flow is underexpanded ($p_{\text{exit}}/p_\infty \sim 3$), and an expansion fan pattern can be seen in the vicinity of the nozzle exit. These results are well explained by conventional gas dynamics and depict expected nozzle flow and plume behavior. Similar results have been obtained for decomposed N_2H_4 simulations. It should be noted that flow details may be less accurate further downstream of the nozzle exit in the exhaust plume owing to rarefaction effects that are not accounted for with a continuum model. However, this fact *does not* affect thrust calculations, which is the focus of this study.

The micronozzle performance is assessed according to the axial momentum flux per unit depth (thrust) produced at the exit plane. The thrust performance results for both of the monopropellants are summarized in Fig. 4. The thrust results are normalized by quasi-1-D inviscid theory (which yields a thrust output of 28.24 μN/μm) for the given flow parameters.

A notable reduction in the thrust output is observed for both of the monopropellants as the expander half-angle is increased above 30 deg, which is a direct consequence of expander geometry. For large expander angles, the flow follows the walls in the expander and, thus, a sizeable component of the velocity vector exits the nozzle in the transverse direction. This results in a significant reduction of axial momentum flux and a corresponding decline in thruster performance.

For small expander angles, the transverse velocity components due to expander geometry are reduced, but at the expense of increased nozzle length to maintain the fixed area expansion ratio. As the expander angle is decreased below 30 deg, the viscous forces acting over the lengthened expander section begin to dominate the nozzle performance. The subsonic layer acts to restrict the flow and diminish the effective exit area, causing a noticeable reduction in the H_2O_2 micronozzle performance. In addition, because the viscous boundary layer at the exit plane is subsonic, the ambient flowfield, geometry, and back pressure can communicate upstream and into the nozzle expander near the walls. Premature flow turning occurs near the micronozzle exit as the flow adjusts to match the external geometry and ambient back pressure. Thus, a portion of the exit momentum is vectored into the transverse direction, which results in a further reduction in the micronozzle performance. These combined effects dominate any performance gains resulting from the axial flow alignment at small angles and, thus, represent a performance tradeoff between the viscous and geometric effects. A consequence of this tradeoff is that the H_2O_2 micronozzle demonstrates a (weak) maximum in performance near $\theta = 30$ deg.

In comparison, the normalized thrust for decomposed N_2H_4 is essentially a constant value of $\sim$0.91 for $\theta \leq 30$ deg. There is not the dominance of viscous forces at small expander angles (as observed for H_2O_2) owing to a virtual balance between the geometric improvements and viscous layer effects at small expander angles. This balance is possible for N_2H_4 flows because its viscosity is $\sim$20% less than that of decomposed H_2O_2 over the temperature range in the micronozzle expander section (Fig. 5).

To provide additional insight into the nature of the viscous effects, the subsonic layer in the nozzle expander can be examined. Figure 6 shows the viscous subsonic layer in the 30-deg expander half-angle for both decomposed H_2O_2 and decomposed N_2H_4. Forming at the throat, the viscous subsonic layer grows as the axial location progresses toward the exit. The subsonic layer thickness also scales with the fluid viscosity, as is evident for the two different monopropellants shown in Fig. 7. Here the steady-state subsonic layer thickness at the nozzle exit has been quantified as a function of the expander half-angle. As the expander angle is decreased, the subsonic layer grows to occupy a larger percentage of the nozzle exit

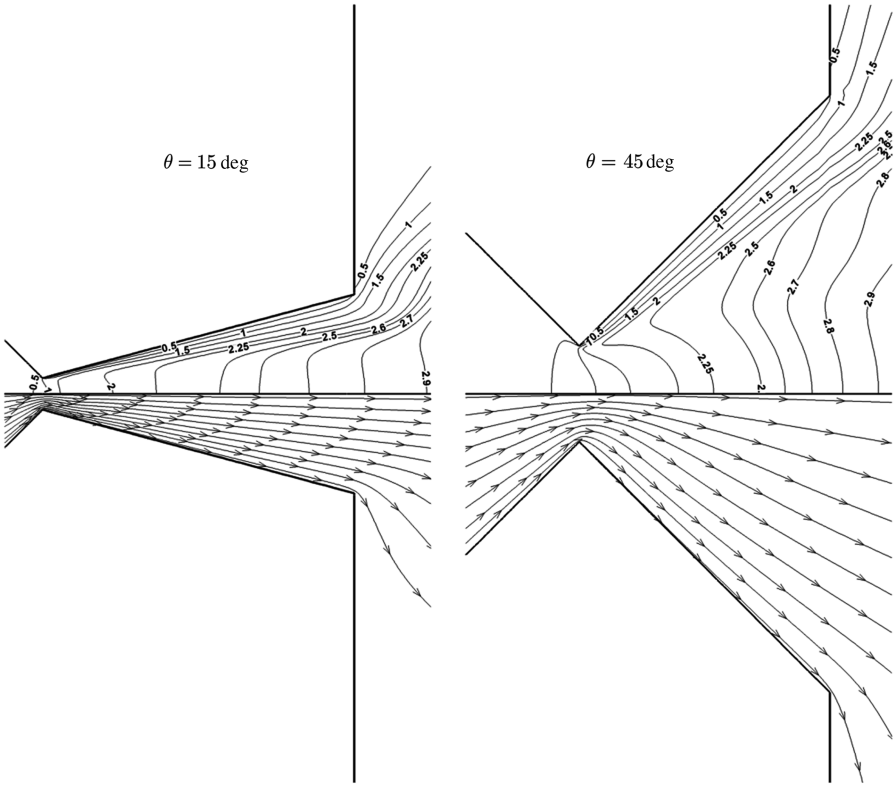

Fig. 3 Plots of the Mach contours and flow streamlines for decomposed hydrogen peroxide at a throat $Re = 800$ for the 15- and 45-deg expander half-angles exhausting to 1 kPa ambient back pressure. Note the expansion fan pattern as a result of the underexpanded supersonic flow conditions at the nozzle exit as well as the increased lateral velocity components at the large expander angles.

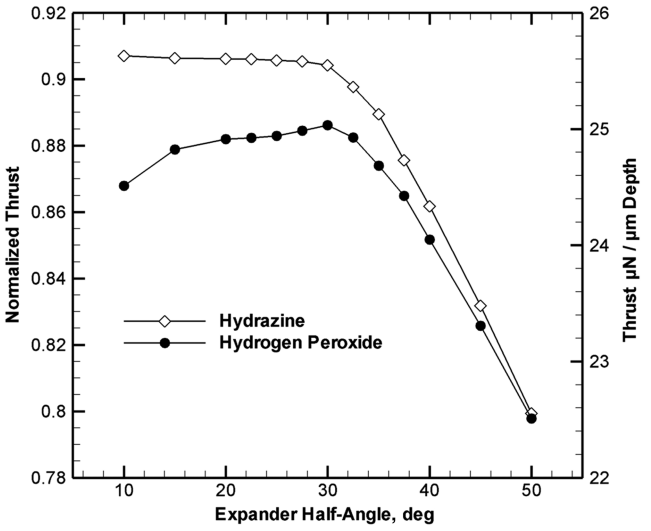

Fig. 4 Plots of thrust output per unit depth as a function of the expander half-angle for decomposed hydrogen peroxide and hydrazine at an inlet to back-pressure ratio of $P_0/P_\infty = 250$. The results have been normalized by quasi-1-D inviscid theory, which yields a thrust value of 28.24 μN per micron depth for the given expansion ratio. Hydrogen peroxide exhibits a weak maximum performance near $\theta = 30$ deg, whereas there is no clear maximum for hydrazine.

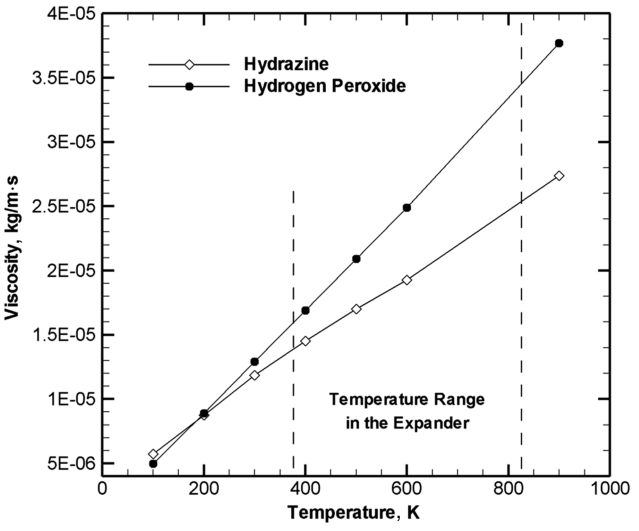

Fig. 5 Plot of the temperature variation in viscosity for the two decomposed monopropellants. The viscosity of decomposed H_2O_2 is, on average, 20% larger than that of decomposed N_2H_4 over the operating temperature range of the micronozzle, and it is more sensitive to changes in temperature.

area, up to 15% for decomposed H_2O_2 and up to 8.5% for decomposed N_2H_4. For cases of smaller expansion angles, the corresponding length of the expander increases, allowing the subsonic layer to grow as the flow moves further downstream. This scenario is directly responsible for the reduction in the performance of the micronozzle at small divergence angles. For larger expander angles, the subsonic layer thickness again increases proportionally. Here the flow is forced to turn sharply at the throat as it enters the micronozzle expander section. The high-speed bulk flow is unable to turn efficiently, and a thick subsonic layer results near the wall boundary. However, owing to the low Reynolds number regime, no flow separation is observed.

B. Performance of Perfectly Expanded Nozzles

The flows considered up to this stage have been underexpanded, which would always be the case in an actual space environment. However, this does not represent the most efficient nozzle operation. Thus, we have chosen to examine how these results are influenced

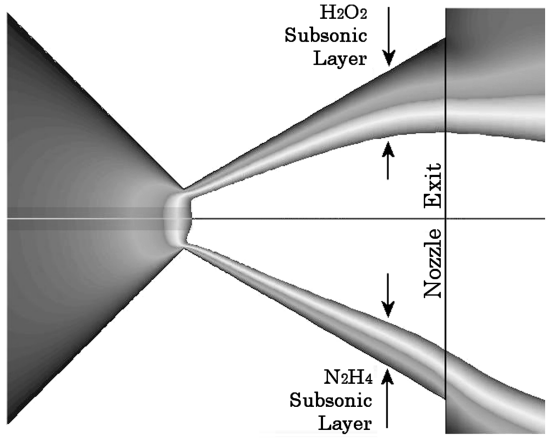

Fig. 6 Plots showing the extent of the subsonic boundary layer for the $\theta = 30$ deg expander for a throat Reynolds number of $Re = 30$. The decomposed H_2O_2 subsonic layer is shown on the top half of the nozzle whereas the decomposed N_2H_4 subsonic layer is shown on the bottom. The size of the subsonic layer, as measured by the arrows, is noticeably larger for the H_2O_2 thruster.

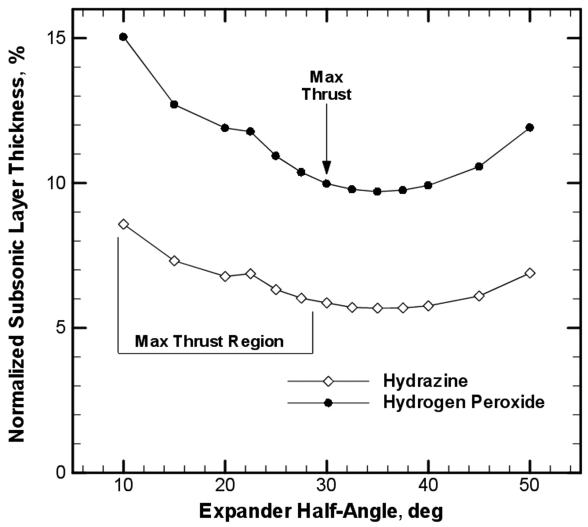

Fig. 7 Plots of the subsonic boundary-layer thickness at the nozzle exit expressed as a percentage of the total micronozzle exit area. The minimum in subsonic layer thickness does not exactly match the thrust maximizing geometry because of the tradeoff between the viscous and geometric losses.

when the nozzle exit flow is ideally expanded (i.e., the pressure is matched to the ambient back-pressure value). For the inlet conditions of the preceding simulations, the required ambient back pressure was estimated from quasi-1-D theory to be ~3.1 kPa. This new back pressure was then applied to the outlet boundary condition and the simulations were repeated.

The comparative thrust results and subsonic layers for decomposed H_2O_2 are shown in Fig. 8 for varying expander angles. As expected, the performance of the perfectly expanded flow is *increased* over virtually all of the expander half-angles. The essential reason is the reduction in the flow turning at the nozzle exit. It is important to note that the optimal expander angle does not change; in fact, the peak becomes more pronounced for the perfectly expanded case.

However, there is actually a *decrease* in the performance at very small expander angles as a result of the viscous effects. The fact that the underexpanded case outperforms the perfectly expanded case for the 10-deg expander half-angle appears counterintuitive from a purely inviscid standpoint. However, taking into account viscous effects and the large subsonic layer seen at very small expander angles, the overall pressure gradient across the nozzle becomes a key factor in determining performance. The subsonic layer accounts for

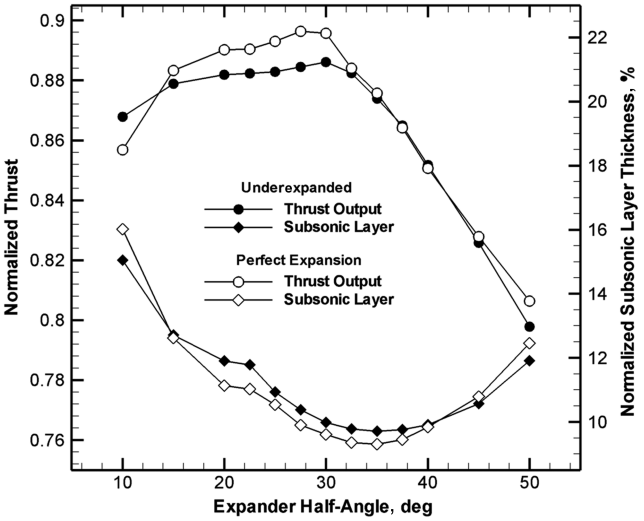

Fig. 8 Comparative plot showing the normalized thrust results and exit subsonic layer size as a percentage of the nozzle exit for both the underexpanded (1.0 kPa back pressure) and perfectly expanded (3.1 kPa back pressure) flow regimes. Decomposed hydrogen peroxide thrust results have been normalized by quasi-1-D inviscid theory, which yields a thrust value of 28.24 μN per micron nozzle depth. The thrust maximizing geometry remains $\theta \sim 30$ deg and the "peak" is more pronounced for the perfectly expanded conditions.

at least 15% of the total flow through the 10-deg micronozzle expander. As such, the increased back pressure of the perfect expansion acts to reduce the overall pressure gradient across the nozzle and thus reduces the mean flow in the subsonic layer. This flow reduction accounts for the performance decrease for the perfectly expanded micronozzles with small expansion angles.

The overall performance increase for the perfectly expanded micronozzle flows is further delineated by an analysis of the viscous subsonic layer. A comparison of the subsonic layer size at the nozzle exit for the perfectly expanded and underexpanded conditions is shown in Fig. 8. For the pressure matched exit flow, the percentage of the exit area occupied by the subsonic layer decreases for the majority of the expander angles. (The exceptions are the extremely large and small half-angles.)

C. Nozzle Performance for Varying Reynolds Numbers

In the preceding simulations, the mass flow rate and, thus, the Reynolds number were maintained at a fixed value ($Re \sim 800$). It is expected that the extent of the viscous subsonic layer will depend on the Reynolds number. Accordingly, we performed simulations over a range of Reynolds numbers spanning from $Re \sim 15$–800; only the 30-deg expander half-angle geometry has been considered. In practice, the range of Reynolds numbers was achieved by controlling the mass flow rate through the nozzle by adjusting the inlet stagnation pressures from 5 to 250 kPa. All of the other boundary conditions and simulation parameters are held constant as previously described.

Figure 9 illustrates the Mach number contours in the micronozzle and exhaust plume at four different values of throat Reynolds numbers (30, 160, 320, and 650) for decomposed H_2O_2. As would be expected, at low Reynolds numbers (inlet pressures), the flow is overexpanded and free boundary shock reflection occurs. As the Reynolds number increases, the flow transitions from the overexpanded through the perfect expansion and finally to the underexpanded exit conditions. At a throat Reynolds number of 15, the supersonic portion of the flow is confined to a small region immediately downstream of the throat. Further downstream, the viscous subsonic layer quickly grows to occupy the entire expander cross section, and the flow transitions back to subsonic conditions. This phenomena is demonstrated in Fig. 10, which shows the relationship between the Reynolds number and the extent of the viscous subsonic layer.

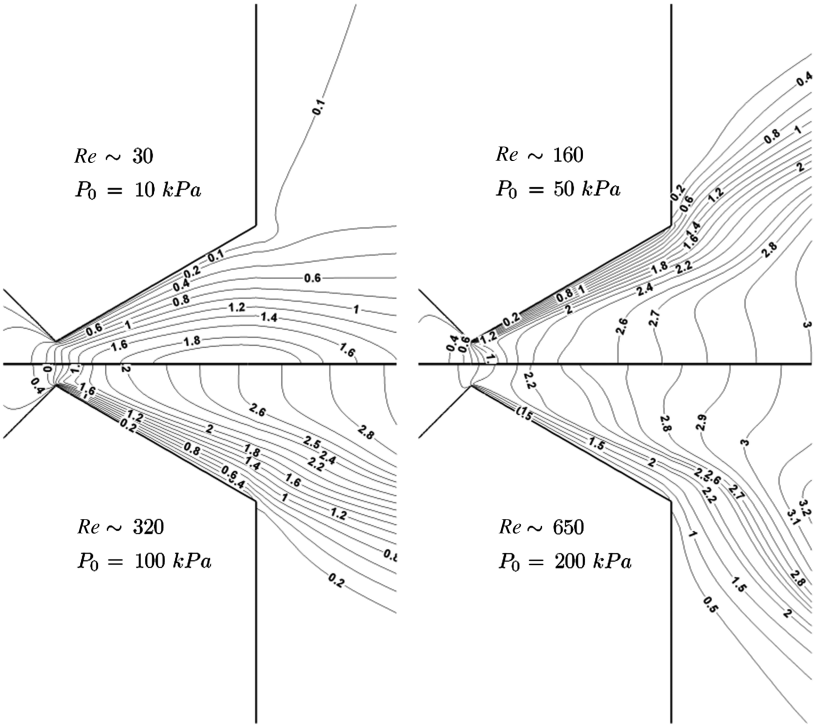

Fig. 9 Mach number contours for the 30-deg divergence half-angle hydrogen peroxide micronozzle for Reynolds numbers of 30, 160, 320, and 650 at the nozzle throat. At low Reynolds numbers, the flow is overexpanded and free boundary shock reflection occurs at the nozzle exit. As the Reynolds number is increased, the flow transitions from over-expanded to underexpanded, and an expansion fan pattern develops at the nozzle exit.

Referring to this figure, it is seen that, as the throat Reynolds number increases ($Re \sim 30$), the viscous forces begin to be offset by the flow inertia, and a significant portion of the flowfield remains supersonic and performance improves. As the Reynolds number increases further, the size of the subsonic layer continues to diminish; however, even for $Re \sim 800$, the subsonic layer can occupy a finite portion of the expander.

An alternative view of the viscous influence at different Reynolds numbers can be given by examining the exit Mach profiles in Fig. 11. According to quasi-1-D inviscid theory, the Mach number is constant at the nozzle exit and depends only on the area expansion ratio. The computed exit Mach profile reflects the subsonic layer thickness at the nozzle exit and, thus, is not constant across the exit plane. The Mach number varies from zero at the nozzle wall and increases with distance from the wall with a maximum value located at the nozzle centerline. As the throat Reynolds number increases, the size of the subsonic layer at the exit decreases and the maximum centerline Mach number increases. Similarly, at higher Reynolds numbers, the exit Mach profiles become more uniform and resemble the constant profile predicted by the 1-D inviscid theory.

D. Nozzle Efficiency and Comparison with Existing Data

As indicated previously, one common measure of the efficiency of a given nozzle design under steady operation is the normalized

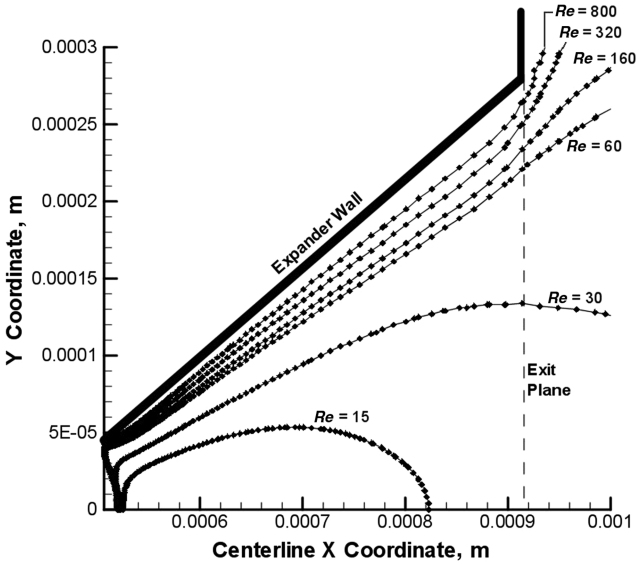

Fig. 10 Plots of the subsonic layer thickness for flow of decomposed H_2O_2 in a 30-deg expander at different Reynolds numbers. The subsonic layer is given by the region between the expander wall and the *Re* curve. The Reynolds number has been varied between $15 < Re < 800$. Note that, as the Reynolds number decreases, the size of the subsonic region increases.

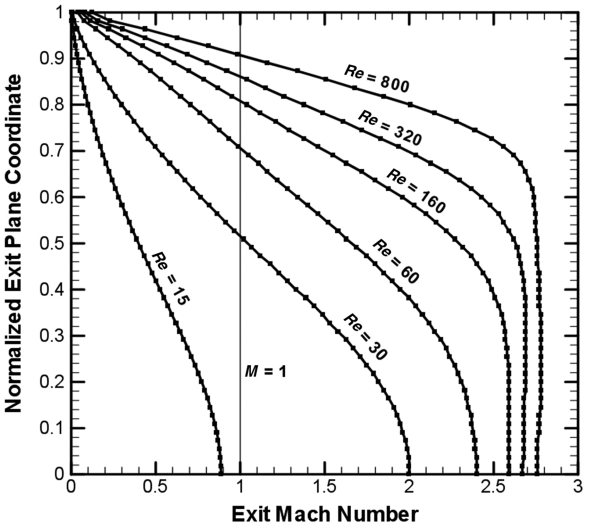

Fig. 11 Mach number profile at the nozzle exit plane for Reynolds numbers between $15 < Re < 800$. The exit plane has been normalized where 0 represents the nozzle centerline and 1 represents the nozzle wall. As the Reynolds number increases, the flow approaches the inviscid regime and the Mach profiles become more uniform in the exit plane.

specific impulse η defined by Eq. (13). A summary of the efficiency estimates from the Reynolds number study are shown in Fig. 12. Here we present the value of η as a function of the throat Reynolds number for decomposed H_2O_2 flows at the 20-, 30-, and 40-deg half-angle expander configurations. It is seen that the efficiency is quite poor at very low throat Reynolds numbers due to the dominance of viscous losses. At a $Re \sim 50$, there is a sharp increase in efficiency. The existence of an optimal expansion angle appears to be most pronounced for throat Reynolds numbers in the range of 100–200, for which it is seen that the maximum performance is actually attained for a wider 40-deg geometry. For larger Reynolds numbers ($\sim$300 or higher) the efficiencies vary by, at most, a few percent. Generally, the 30-deg expander yields the highest efficiency; however, beyond a Reynolds number of 600, the efficiencies are nearly indistinguishable between the 20- and 30-deg expander geometries. It is important to bear in mind that these efficiencies are likely to be overestimates of an actual 3-D device performance due to the 2-D nature of the simulations. We will return to this point in the Sec. IV.

The characterization of the micronozzle efficiency also affords an opportunity to compare our results with existing numerical and experimental data in the aerospace literature. Comparisons are inherently limited in their scope because most of the available data pertains to conical micronozzles with hot and cold gas propulsion schemes (N_2, He). No data appear in the literature for the monopropellant schemes addressed in this paper. The primary sources for comparisons are found in the DSMC studies by Alexeenko et al. [9–13] and the joint experimental/computational (DSMC) paper by Ketsdever et al [14]. Experimental data are especially limited, with Ketsdever et al. [14] being the sole source; furthermore, those experimental data are restricted to extremely low Reynolds number flows ($Re < 20$) of cold gas (He). Using the available data from these references, we have computed the corresponding micronozzle efficiencies, and the data appear in Fig. 12 along with our 2-D numerical results. The data comparison suggests several observations. First, our 2-D simulations agree extremely well with the cold gas experiments at a very low Reynolds number ($Re \sim 15$). This level of agreement, despite the different geometries, is most likely attributed to the fact that the supersonic portion of the flow at this low Reynolds number is mostly confined to the centerline region of the expander and well away from the solid boundaries. Second, the DSMC hot gas efficiencies are noticeably lower than our results, as would be expected due to their use of an axisymmetric geometry as compared with our 2-D geometry.

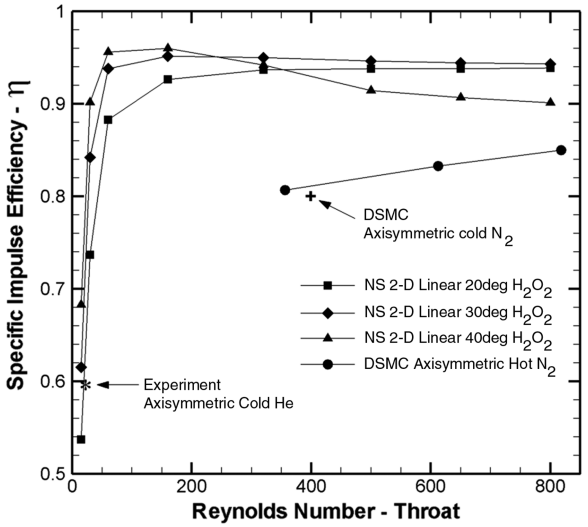

Fig. 12 A summary plot depicting calculated micronozzle efficiencies η as a function of the throat Reynolds number for decomposed H_2O_2 and different nozzle expander half-angles of 20, 30, and 40 deg. Also shown for comparison are related experimental and numerical data from the literature for conical micronozzle flows. The DSMC data represent hot and cold N_2 gas flows [12] and the experimental data are for a cold He gas flow [14].

However, the DSMC results do indicate a relatively weak Reynolds number dependence at higher values ($Re > 300$), which is consistent with our findings. Lastly, the DSMC results for conical, cold He micronozzle flow from Ketsdever et al. [14] showed that for $Re = 60$ the highest efficiency was obtained for a 40-deg nozzle half-angle, whereas, at $Re = 200$ the 30-deg nozzle exhibits maximum efficiency. This, too, is consistent with our results in Fig. 12.

E. Impact of Monopropellant Thermophysical Properties

Last, we consider the specific effects of temperature-dependent thermophysical properties and, specifically, the viscosity of the decomposed monopropellants in the micronozzle flow. Here we compare the flows of decomposed H_2O_2 and N_2H_4 to explore the influence of the temperature-dependent viscosity on the size of the subsonic layer. Identical throat Reynolds numbers were established through control of the pressure inlet boundary condition. The throat

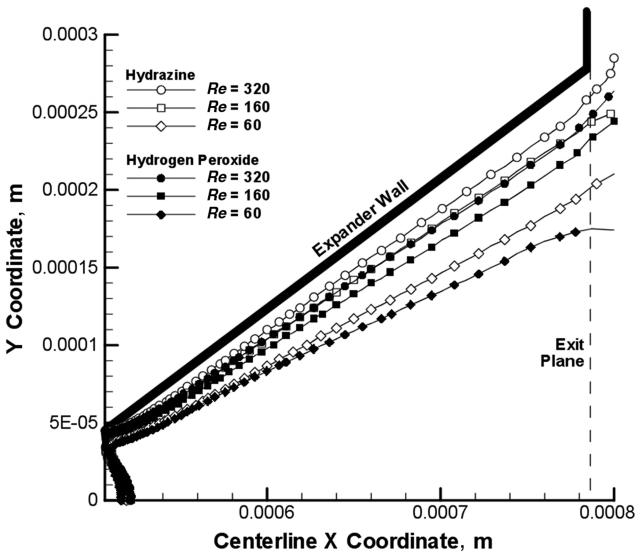

Fig. 13 A plot showing a comparison of the subsonic boundary-layer growth in the nozzle expander for both decomposed monopropellants. The two working fluids are compared at equivalent throat Reynolds numbers of 60, 160, and 320. The layers are similar in the vicinity of the throat. However, as the flow moves downstream in the expander, the Reynolds number grows more quickly for N_2H_4 and, thus, the subsonic layer is smaller compared with H_2O_2.

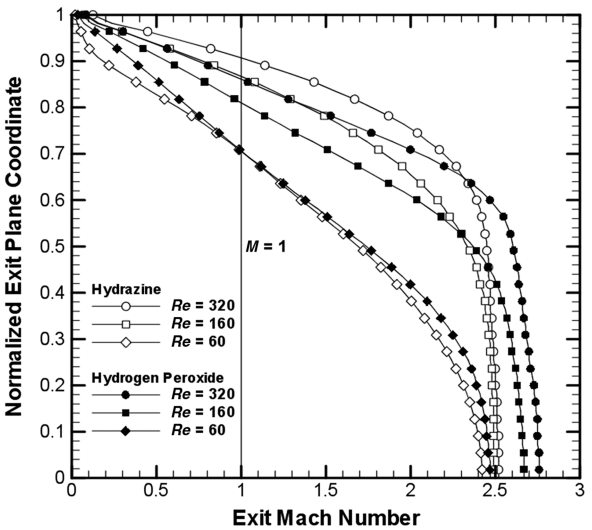

Fig. 14 Plot of the Mach number profile at the nozzle exit plane for the two different monopropellant flows with throat Reynolds numbers of 60, 160, and 320. The more pronounced viscous effects of H_2O_2 are evident.

Reynolds numbers, though not precisely known a priori, are well estimated using a combination of quasi-1-D nozzle theory, the mass flow relation equation (5), and the temperature-dependent viscosity (Fig. 5). This estimate was found to give quite satisfactory results.

Figure 13 compares the size of the subsonic layer in the expander for both of the decomposed monopropellants at throat Reynolds numbers of 60, 160, and 320. Qualitatively, the subsonic layers show a similar development in the expander. For a given Reynolds number, the subsonic layers for both of the monopropellants are indistinguishable in the vicinity of the throat region. However, the discrepancy between the subsonic layers grows with the downstream position; our results indicate as much as a 13% difference exists for the cases examined. The discrepancy is most pronounced at the lowest Reynolds numbers.

At low Reynolds numbers, the viscous effects cause the flow to essentially stagnate along the expander walls. As a result, the local temperature in the near wall region rises, which concurrently increases viscosity (Fig. 5). The inherently larger viscosity of decomposed H_2O_2 results in an expander wall temperature that is approximately twice that of decomposed N_2H_4 in our simulations. As the viscosity increases with temperature, so does the extent of the subsonic layer and, thus, a greater portion of the near wall flow is decelerated. Moreover, as the sonic velocity also increases with the wall temperature, the local Mach numbers near the wall will decrease, thus resulting in increased subsonic layer growth. This represents a twofold positive feedback mechanism for viscous subsonic layer growth that is inherent to realistic monopropellants with temperature-dependent viscosities. From Fig. 5 it can be seen that the viscosity of decomposed H_2O_2 is more sensitive to temperature changes compared with decomposed N_2H_4. As a result, for equivalent throat Reynolds numbers, the size of the decomposed H_2O_2 subsonic layer is larger than the decomposed N_2H_4 subsonic layer throughout the entire length of the micronozzle expander. These concepts are illustrated in Fig. 14, which shows the Mach number profiles at the exit plane for both of the monopropellants of interest.

IV. Conclusions

Supersonic micronozzle flow represents a unique flow regime characterized by supersonic Mach numbers and low Reynolds numbers. In this study, our goal has been to delineate the interactions between the viscous forces and nozzle geometry to better understand thrust production and nozzle performance on the microscale. The specific contributions of this work include detailed examinations of the following: 1) a variable nozzle geometry (expander half-angles 10–50 deg), 2) an extended range of flow Reynolds numbers between 15–800, and 3) the simulation of realistic decomposed monopropellants (H_2O_2, N_2H_4).

The numerical results indicate that tradeoffs exist between the size of the viscous subsonic "boundary" layer and geometric losses in thrust due to nonaxial flow components. It is found that the maximum thrust production occurs at an expander half-angle of approximately 30 deg with decomposed H_2O_2 as the monopropellant; this value is significantly larger (2×) than typical half-angles used in macroscale conical thrusters (e.g., Humble et al. [21]). Although the N_2H_4 monopropellant thruster does not exhibit a true maximum thrust output corresponding to a specific geometry, it is clear that the most effective half-angle is in the range of 25 deg and less. These findings are consistent with the results for cold gas micronozzles reported in Ketsdever et al. [14].

The simulation data for the H_2O_2-based micronozzle show that the efficiency drops off dramatically for $Re \lesssim 100$ and remains nearly constant at 90% for $Re \gtrsim 200$. It is important to note that these efficiencies are likely to be artificially high owing to the 2-D planar nature of our model. In practice, MEMS-based nozzles will be three dimensional, and the depth direction will introduce two additional solid boundaries that will give rise to additional viscous losses [22]. The severity of these additional losses will certainly depend on the depth of the nozzle. Further details regarding the performance of 3-D linear micronozzles will appear in a forthcoming paper.

Acknowledgment

This work was supported by the United States Air Force Office of Sponsored Research (AFOSR) under grants FA49620-02-1-0230 and FA9550-06-1-0364.

References

[1] Blandino, J., and Cassady, R., "Propulsion Requirements and Options for the New Millennium Interferometer (DS-3) Mission," AIAA Paper 98-3331, 1998.

[2] Pollard, J., Chao, C., and Janson, S., "Populating and Maintaining Cluster Constellations in Low-Earth Orbit," AIAA Paper 99-2871, 1999.

[3] Mueller, J., "Thruster Options for Micro-Spacecraft: A Review and Evaluation of the State-of-the-Art and Emerging Technologies," *Micropropulsion for Small Spacecraft -Progress in Astronautics and Aeronautics*, edited by M. Micci, and A. Ketsdever, Vol. 187, AIAA, Reston, VA, 2000, pp. 45–137.

[4] Reichbach, J. G., Sedwick, R. J., and Martinez-Sanchez, M., "Micropropulsion System Selection for Precision Formation Flying Satellites," AIAA Paper 2001-3646, 2001.

[5] Hitt, D. L., Zakrzwski, C., and Thomas, M., "MEMS-Based Satellite Micropropulsion via Catalyzed Hydrogen Peroxide Decomposition," *Smart Materials and Structures*, Vol. 10, No. 6, Dec. 2001, pp. 1163–1175.
doi:10.1088/0964-1726/10/6/305

[6] Bayt, R. L., and Breuer, K. S., "Viscous Effects in Supersonic MEMS-Fabricated Micronozzles," *Proceedings of the 3rd ASME Microfluids Symposium*, American Society of Mechanical Engineers, New York, 1998.

[7] Bayt, R. L., and Breuer, K. S., "System Design and Performance of Hot and Cold Supersonic Micro-Jets," AIAA Paper 2001-0721, 2001.

[8] Alexeenko, A. A., Levin, D. A., Gimelshein, S. F., and Collins, R. J., "Numerical Modeling of Axisymmetric and Three-Dimensional Flows in MEMS Nozzles," *Proceedings of the 36th AIAA/ASME/SAE/ASEE Joint Propulsion Conference*, AIAA, Reston, VA, 2000.

[9] Alexeenko, A. A., Levin, D. A., Gimelshein, S. F., Collins, R. J., and Reed, B. D., "Numerical Modeling of Axisymmetric and Three-Dimensional Flows in Microelectromechanical Systems Nozzles" *AIAA Journal* Vol. 40, No. 5, May 2002, pp. 897–904.

[10] Alexeenko, A., Levin, D., Collins, R. J., and Markelov, G. N., "Numerical Simulation of High Temperature Gas Flows in a Millimeter-Scale Thruster," *Journal of Thermophysics and Heat Transfer*, Vol. 16, No. 1, 2002, pp. 10–16.

[11] Alexeenko, A.A., Gimelshein, S. F., Levin, D. A., Ketsdever, A. D., and Ivanov, M. S., "Measurements and Simulation of Orifice Flow for Micropropulsion Testing," *Journal of Propulsion and Power*, Vol. 19, No. 4, July 2003, pp. 588–594.

[12] Alexeenko, A. A., Levin, D. A., Fedosov, D. A., Gimelshein, S. F., and Collins, R. J., "Performance Analysis of Microthrusters Based on Coupled Thermal-Fluid Modeling and Simulation," *Journal of Propulsion and Power*, Vol. 21, No. 1, 2005, pp. 95–101.
doi:10.2514/1.5354

[13] Alexeenko, A. A., Fedosov, D. A., Gimelshein, S. F., Levin, D. A., and Collins, R. J., "Transient Heat Transfer and Gas Flow in a MEMS-Based Thruster," *Journal of Microelectromechanical Systems*, Vol. 15, No 1, 2006, pp. 181–194.
doi:10.1109/JMEMS.2005.859203

[14] Ketsdever, A. D., Clabough, M. T., Gimelshein, S. F., and Alexeenko, A., "Experimental and Numerical Determination of Micropropulsion Device Efficiencies at Low Reynolds Numbers," *AIAA Journal*, Vol. 43, No. 3 March 2005, pp. 633–641.
doi:10.2514/1.10284

[15] Choudhuri, A. R., Baird, B., Gollahalli, S. R., and Schneider, S. J., "Effects of Geometry and Ambient Pressure on Micronozzle Flow," *Proceedings of the 37th AIAA/ASME/SAE/ASEE Joint Propulsion Conference*, AIAA, Reston, VA, 2001.

[16] Mueller, J., "Review and Applicability Assessment of MEMS-Based Microvalve Technologies for Microspacecraft Propulsion," *Micropropulsion for Small Spacecraft*, edited by M. Micci, and A. Ketsdever, Vol. 187, Progress in Astronautics and Aeronautics, AIAA, Reston, VA, 2000, pp. 449–476.

[17] Vargaftik, N. B., *Thermophysical Properties of Gases and Liquids*, 2nd ed., Hemisphere, New York, 1975.

[18] Anderson, J. D., Jr., *Modern Compressible Flow with Historical Perspective*, 3rd ed., McGraw–Hill, Boston, 2003.

[19] Arkilic, E., Breuer, K., and Schmidt, M., "Mass Flow and Tangential Momentum Accommodation in Silicon Micromachined Channels,"

Journal of Fluid Mechanics, Vol. 437, No. 29, 2001, pp. 29–44. doi:10.1017/S0022112001004128

[20] Saad, M. A., *Compressible Fluid Flow*, 2nd ed., Prentice–Hall, New York, NY, 2003.

[21] Humble, R. W., Henry, G. N., and Larson, W. J., *Space Propulsion Analysis and Design* McGraw–Hill, New York, 1995.

[22] Louisos, W., and Hitt, D., "Heat Transfer & Viscous Effects in 2D & 3D Supersonic Micro-Nozzle Flows," AIAA Paper 200-3987, 2007.

T. Lin
Associate Editor